

Unsupervised Iterative U-Net with an Internal Guidance Layer for Vertebrae Contrast Enhancement in Chest X-Ray Images

Ella Eidlin, Assaf Hoogi, Nathan S. Netanyahu

Abstract—X-ray imaging is a fundamental clinical tool for screening and diagnosing various diseases. However, the spatial resolution of radiographs is often limited, making it challenging to diagnose small image details and leading to difficulties in identifying vertebrae anomalies at an early stage in chest radiographs. To address this limitation, we propose a novel and robust approach to significantly improve the quality of X-ray images by iteratively training a deep neural network. Our framework includes an embedded internal guidance layer that enhances the fine structures of spinal vertebrae in chest X-ray images through fully unsupervised training, utilizing an iterative procedure that employs the same network architecture in each enhancement phase. Additionally, we have designed an optimized loss function that accurately identifies object boundaries and enhances spinal features, thereby further enhancing the quality of the images. Experimental results demonstrate that our proposed method surpasses existing detail enhancement methods in terms of BRISQUE scores, and is comparable in terms of LPC-SI. Furthermore, our approach exhibits superior performance in restoring hidden fine structures, as evidenced by our qualitative results. This innovative approach has the potential to significantly enhance the diagnostic accuracy and early detection of diseases, making it a promising advancement in X-ray imaging technology.

Index Terms—Loss optimization, Image enhancement, X-Ray screening, Spinal Cord, Deep Learning

I. INTRODUCTION

X-RAY screening is a widely used and indispensable imaging modality in clinical practice for diagnosing a variety of pathologies. From a single chest X-ray image, radiologists can identify pleural disorders, aortic abnormalities, vertebral height loss, orthopedic surgery, osteopenia, scoliosis, and more [1]. However, the limited spatial resolution of X-ray images can result in inaccurate diagnoses, particularly in cases of vertebral fractures [2]. This limitation can be attributed to various factors, including poor equipment performance, which may necessitate the use of more costly and time-consuming imaging modalities like magnetic resonance imaging (MRI). However, MRI may not always be feasible, especially in emergency rooms where time is critical for accurate diagnosis and prompt treatment. Additionally, the ability to obtain a comprehensive diagnosis, including lung and back anomalies, from a single chest X-ray without the need for additional vertebrae X-ray can be immensely valuable in emergency settings. Rapid and accurate diagnosis is crucial in emergency

Ella Eidlin is with the Department of Computer Science, Bar Ilan University, Ramat Gan, Israel (e-mail: ella.0519@gmail.com).

Assaf Hoogi is with the Department of Computer Science, Ariel University, Ariel, Israel (e-mail: ahoogi@gmail.com).

Nathan S. Netanyahu is with the Department of Computer Science, Bar Ilan University, Ramat Gan, Israel (e-mail: nathan@cs.biu.ac.il).

care to ensure timely and appropriate interventions. Therefore, the demand for innovative solutions to enhance the spatial resolution and diagnostic accuracy of X-ray images is urgent and paramount, as it has the potential to significantly improve patient care and outcomes, particularly in emergency situations.

Numerous techniques have been proposed for enhancing the quality of medical images, including conventional methods like edge-aware filters [1], histogram equalization, gamma correction [2], or Contrast Limited Adaptive Histogram Equalization (CLAHE) [3]. However, these techniques may only improve the contrast or brightness of X-ray images, often at the cost of losing important image details [4]. Other approaches, such as supervised super-resolution [5], [6], [7], [8], can enhance fine details, but they require labeled instances, which is a laborious, expensive, and time-consuming process. Moreover, obtaining high-quality supervision may be challenging in many medical image cases. This fundamental challenge poses a significant obstacle in the field of medical imaging, demanding innovative and efficient solutions to overcome these limitations.

Existing unsupervised methods for super-resolution tasks help to enhance fine image details. These methods can be broadly categorized into self-supervised approaches [9] and those based on Generative Adversarial Networks (GANs), such as CinCGAN [10], or autoencoder-based models like the dSRVAE model [11]. However, these methods may not be optimized for medical images, which often exhibit unique features and are acquired under varying conditions. In addition, in order to obtain an accurate super resolution solution, the downscaling kernel should be known/accurately assessed - difficult in the medical domain. Therefore, the use of super-resolution techniques that are not specifically designed for the medical domain can be detrimental, as they may introduce or remove information from the images, leading to potential inaccuracies. For instance, the dSRVAE model employs perceptual loss to improve high-frequency reconstruction, which may not be suitable for medical images as it can risk introducing unwanted features. In the CinCGAN model, the first cycle of the architecture uses total variation (TV) loss for noise removal and smoothness enhancement, which may result in the loss or blurring of fine details, making them challenging to visualize. Therefore, there is a critical need for tailored super-resolution methods that are specifically designed for medical images to ensure accurate and reliable results.

Gozes [12] proposed a supervised learning approach for improving bone radiographs, which is one of the few available methods to improve fine details visualization in x-ray images.

This method was developed to enhance bone structures and was trained on synthetically generated datasets using the Digitally Reconstructed Radiograph (DRR) technique. While the method is capable of generalizing to low-quality X-ray bone structures, its effectiveness is limited by the quality of the high-quality radiographs in the synthetic dataset. Furthermore, the method involves a complex and laborious process for generating and extracting the enhanced skeleton.

In this paper, we introduce a novel method for enhancing the spine vertebrae structures in chest radiographs. The proposed method presents the following key-contributions -

- As far as we know, this is the first **fully unsupervised and iterative U-Net training for medical image improvement**. Unlike traditional supervised U-Net training, here it is trained as a generative model in an unsupervised manner. Therefore, the proposed model **can improve a label-free data, solving one of the main challenges in the medical domain** (limited training data).
- To the best of our knowledge, this is the first methodology in the medical field that has **an internal guidance layer**, instead of an external layer or knowledge distillation.
- In this study, **we introduce a novel weighted loss function that combines two distinct types of losses, each capturing varying levels of image information**. The details enhancement loss, which is based on weak supervision, is utilized to enhance the clarity of local objects. Meanwhile, the gradient correlation-based loss is designed to improve the accuracy of borders in high-frequency objects.

The rest of the paper presents the proposed method in section III. The experimental results and ablation study appear in section IV, and the conclusions are in section V.

II. RELATED WORK

A. Traditional Image Enhancement Methods

Ali *et al.* [13] proposes a new approach using an iterative, mean, and multi-threshold selection criterion with plateau limits, which includes histogram segmentation, clipping, and transformation modules. The histogram partition uses multiple thresholding processes to divide the histogram into two parts, and the clipping process enhances contrast by controlling the rate of enhancement. Histogram equalization is then applied to each segmented sub-histogram to preserve brightness and enhance contrast. However, a key limitation of this method is that it does not consider the spatial relationship between adjacent pixels in the image, which can result in the loss of important details.

Fattal and colleagues [14] presented an image enhancement method aimed at improving image quality by manipulating image details at multiple scales. The method involves decomposing an image into various scales, where each scale represents a different level of detail. A weighted least squares filter (WLS) is then used to smooth the image while preserving edges, and the decomposition technique is applied to various

scales of the image, allowing for the manipulation of details at different levels. However, this method requires images to have distinct edges and textures, which may not be easily discernible in low-contrast medical images such as X-rays.

B. Learning-based Image Enhancement Methods

In [15], Madmad *et al.* proposed a learning-based model for enhancing X-ray image details. The method utilizes a convolutional neural network with two branches, which are trained on a synthetic dataset. This dataset consists of two sets of images: the first set includes elliptic and rectangular geometric shapes that simulate background objects, such as lungs, in X-ray images, while the second set contains local structures resembling nodules, fractures, and lung pipes. The network decomposes the input image into its geometric shapes and local structures and trains each branch simultaneously. The model's objective is to reconstruct the original input image by summing the outputs of the two branches. However, the generalizability of the proposed method may be limited due to the narrow variety of images in the training dataset.

Sander *et al.* presented an unsupervised learning-based approach to enhance the resolution of medical images, as elaborated in [16]. The method is specifically designed to address anisotropic artifacts frequently observed in CT or MR scans that may result in incorrect diagnoses. The primary idea behind the proposed approach is to utilize the autoencoder's latent space interpolation capability to generate high-resolution images. Notably, the model was exclusively trained on anisotropic MR scans, which could limit its generalization capability to other types of medical images.

Ma *et al.* proposed a super-resolution method that utilizes image gradient maps to guide image reconstruction, as outlined in [17]. This fully supervised model is based on a generative adversarial network, consisting of two branches. The first branch is designed to preserve the structural features of the image, while the second branch focuses on the gradient information. The structure-preserving branch can be any standard architecture, and the output is fused with the output from the gradient branch. The gradient branch translates the low-resolution gradient map into a high-resolution gradient map, with intermediate outputs integrated into feature maps from the structure-preserving branch.

III. THE PROPOSED METHOD

A. Preprocessing

The objective of the image preprocessing step is to enhance important features in order to enable more effective learning. One common technique to accentuate the local objects in an image is to increase the contrast of the shapes inside. Therefore, as a first step we incorporate a common practice normalization of image pixels to a specific range, using min-max normalization. Then we apply three additional steps that are illustrated in Figure 1. The first step entails the inversion of the original image $I(x)$ by subtracting its mean $\bar{I}(x)$ from $I(x)$. This process yields negative pixel values in regions where the pixel values are higher than the mean, and positive

pixel values in regions where the pixel values are lower than the mean. The inverted image, denoted as $\tilde{I}(X)$, is defined as follows:

$$\tilde{I}(x) = \bar{I}(x) - I(x) \quad (1)$$

The second step of the proposed method involve a weighted least squares filter (WLS) [14]. The WLS filter is a non-linear technique that balances blurring and sharpening, producing a smooth image while preserving significant features such as edges and textures. The filtered image S is given by:

$$S = \frac{I}{(\mathbb{I} + \lambda A)} \quad (2)$$

where \mathbb{I} is the identity matrix, A is the spatially-varying Laplacian matrix and λ is responsible for the balance between the two terms. For our settings, we set $\lambda = 0.8$. Then, the WLS is formulated as:

$$WLS(S) = \arg \min_S (\|S - I\|_2^2 + \lambda(w_x \frac{\partial S}{\partial x} + w_y \frac{\partial S}{\partial y})) \quad (3)$$

The WLS expression consists of two parts that serve different purposes. The first part, expressed as $\|S - I\|_2^2$, measures the similarity between the original image I and the filtered image S . The second part, given by $\lambda(w_x \frac{\partial S}{\partial x} + w_y \frac{\partial S}{\partial y})$, aims to achieve image smoothing by minimizing the partial derivatives of S . The horizontal and vertical smoothing weights, w_x and w_y , are calculated as exponential expressions of the partial derivatives of the log-luminance channel of the image, which determine the rate of change of image intensity. These weights indicate the level of smoothness in the image and are defined in a manner similar to that used in previous work [18].

$$w_{x,\nu} = \left(\left| \frac{\partial l}{\partial x}(\nu) \right|^\alpha + \varepsilon \right)^{-1}, \quad w_{y,\nu} = \left(\left| \frac{\partial l}{\partial y}(\nu) \right|^\alpha + \varepsilon \right)^{-1} \quad (4)$$

where l is the log-luminance channel of the I , ν is the spatial location of the pixel, α is an exponent in the range $1.2 < \alpha < 2.0$ that determines the sensitivity to the gradients of I , ε is small constant for numeric stability (typically 0.0001).

The combination of the filtered image $WLS(S)$ and the inverted image $\tilde{I}(X)$ results in an inverted image with intensified features. In darker regions, the pixel values are higher, while in brighter regions, they are lower due to negative pixels from $\tilde{I}(X)$. The combination of these two components is defined as follows:

$$P(x) = WLS(S) + \tilde{I}(x) \quad (5)$$

In the last step, the original image is divided by $P(x)$, which highlights the regions where the pixel values of the original image are greater than the mean value and reduce the pixel values in regions where the original image has values smaller than the mean value.

$$E(x) = \frac{I(x)}{P(x)} \quad (6)$$

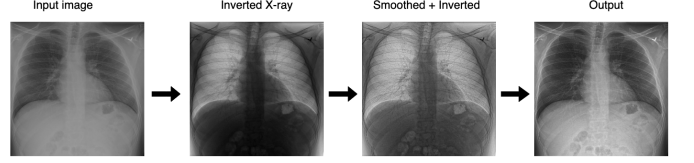


Figure 1: Flow of pre-processing method.

B. Learning-based phase

The proposed approach is able to recover missing details and refine fine structures in a recursive manner. The model incorporate U-Net architecture, originally proposed for medical image tasks such as segmentation [19], super resolution [20], and image enhancement [15], [21]. U-Net's ability to extract multi-scaled features via skip connections allows to perform well on small datasets. Our model uses a single U-Net architecture with embedded guidance, as shown in Figure 4(a), and is trained over three iterations, although the best results were obtained after two. In the first step, the model enhances the overall image visualization and exposes hidden structures in the spinal area. In the second step, the model identifies and captures more complex and fine structures based on the results of the previous step, leading to improved accuracy. The recurrent refinement model is mathematically formulated as follows:

$$x^t = UNet(x^{t-1}) \quad (7)$$

where x^t is the t -th output of the network and $x^0 = x$ which is original input.

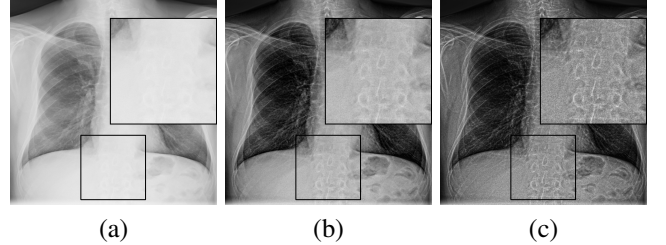


Figure 2: Comparison between results after two learning steps
(a) Original image (b) Image after first enhancement step (c) Image after the second enhancement step.

C. Guidance Layer

Various auxiliary guidance techniques, such as independent guidance branches [17], [8] and sub-networks [5], have been proposed for improving the performance of learning architectures. These approaches involve external knowledge or auxiliary networks, which increase computational costs and

require additional hyper-parameters tweaking. In contrast, our proposed guidance layer is directly embedded in the decoder module and does not require knowledge distillation or external guidance. During the downsampling process in the encoder module, high-frequency image information is lost, makes it challenging to complete the missing details. To address this issue, we proposed a guidance layer (Figure 4(b)) that gradually upsamples during the decoding path (Figure 4(a)). After each training step, the guidance layer is updated with a more detailed information derived from the improved input, leading to greater accuracy in upsampling and specifically focusing on the spinal column vertebrae. The guidance layer is composed of a Leaky Rectified Linear Unit (LeakyReLU) activation function, a convolution layer for detailed feature extraction, and a max pooling layer for adjusting the spatial size of the layer to match the network dimensions. An embedded guidance layer is designed to be an integral part of the main network and is trained jointly with the other layers. This means that the guidance layer can directly influence the activation patterns of the other layers, allowing it to modulate the information flow and representation within the network. As a result, the guidance layer can help to preserve information by providing additional constraints and regularization that encourage the model to learn more structured and informative representations.

Ultimately, the guidance layer is combined with the upsampled convolution layers, wherein each layer assigns a weight based on the empirically determined parameters $\beta = 0.6$ and $1 - \beta = 0.4$. This weighting scheme effectively highlights the relevance of the detail layer, while simultaneously preserving the salient features of the convolutional layer.

D. Loss function

Our loss function targets the enhancement of image details, and at the same time it aims to improve the accuracy of structures borders.

Feature Enhancement. To improve the visibility of desired structures at the spinal region, a feature-based loss is applied. Low-level features are extracted from the 1st layer of the neural network, providing valuable global information and revealing underlying structural details. To leverage these properties for structural enhancement, we first convert all extracted feature maps from the first layer of the network to grayscale images. Next, we calculate a histogram for each feature map to represent the distribution of pixels intensities. In order to quantify the richness of image information, we apply the concept of information entropy, which is a measure of the amount of information contained in the image. Finally, we select the feature map with the highest entropy value, denoted as F , as the most informative image. Figure 3 provides an overview of the process of feature map extraction for the proposed loss function.

By following these steps, we are able to effectively leverage the low-level features in the neural network to enhance the visibility of desired structures in the spinal region.

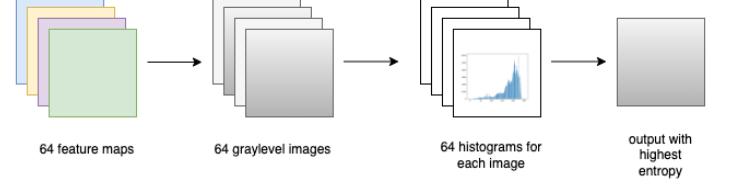


Figure 3: The schematic representation of the feature map extraction for the feature-based loss function.

The feature-based loss is defined as:

$$L_1(x^t, F) = \frac{1}{n} \frac{1}{m} \sum_{i=1}^n \sum_{j=1}^m (x_{(i,j)}^t - F_{(i,j)})^2 \quad (8)$$

where x^t is the input image in t -th training step.

Structural Boundaries Accuracy. To improve the accuracy at the structural boundaries and emphasize the borders of local structures we added gradient-correlation loss between the processed image and the details layer of the input image.

The gradient correlation (GC) [22] metric has been widely used in medical image registration and has demonstrated its effectiveness in improving boundary accuracy in medical images [23].

The GC metric is defined by the normalized cross-correlation between two images. The metric is formulated as follows:

$$NCC(X, Y) = \frac{\sum_{(i,j)} (X - \bar{X})^2 (Y - \bar{Y})^2}{\sqrt{\sum_{(i,j)} (X - \bar{X})^2} \sqrt{\sum_{(i,j)} (Y - \bar{Y})^2}} \quad (9)$$

where X and Y are input images, \bar{X} is average of X image and \bar{Y} is average of Y image.

The final result of the GC metric is obtained by taking the average of the normalized cross-correlation values across both horizontal and vertical directions of the two images, X and Y .

$$GC(X, Y) = \frac{1}{2} [NCC(\nabla g_x X, \nabla g_x Y) + NCC(\nabla g_y X, \nabla g_y Y)] \quad (10)$$

By minimizing this discrepancy during training, the neural network can learn to produce images that are more similar to the desired images in terms of their gradient correlation. The discrepancy between these two images gradients is determined by:

$$L_2(x^t, y^{d,t}) = 1 - GC(x^t, y^{d,t}) \quad (11)$$

where $y^{d,t}$ is details layer in the t -th training step.

The overall objective function is obtained as the sum of the individual loss functions and is mathematically defined as follows:

$$L = \lambda_1 L_1 + \lambda_2 L_2 \quad (12)$$

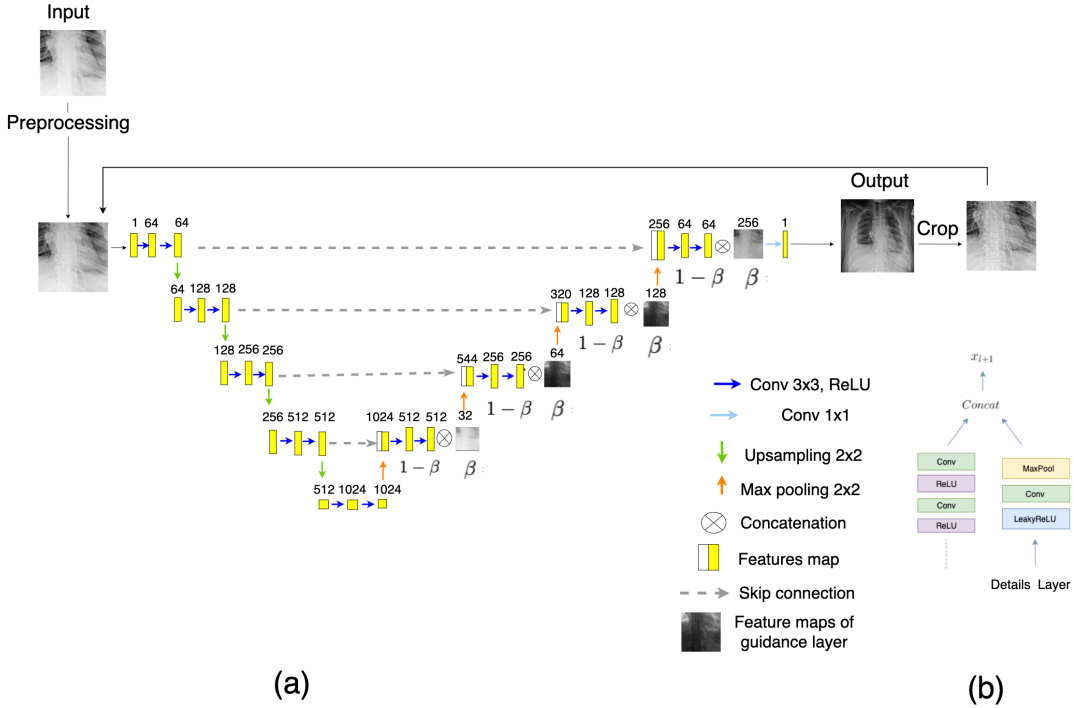


Figure 4: The proposed approach of iterative learning (a) U-Net network with guidance layer (b) Guidance layer concatenated with features layer.

IV. EXPERIMENTS AND ANALYSIS

A. Datasets

To assess the performance of our proposed model, three datasets were utilized: the NIH ChestX-ray14 [24], CheXpert [25], and the JSRT benchmark [26]. The NIH ChestX-ray14 dataset is comprised of 112,120 grayscale X-ray images collected from 30,805 patients, with each image having a dimension of 1024x1024 pixels and a bit depth of 8 bits per pixel. The dataset was labeled for different thoracic organ diseases such as lungs and heart. The CheXpert dataset is a large open-source dataset of multi-label chest X-ray images with different sizes and with an 8-bit depth per pixel. The dataset consists of 224,316 chest radiographs coming from 65,240 unique patients. The dataset is annotated using ground truth labels that were automatically extracted from radiology reports. The annotations corresponding to a label space consisting of 14 radiological observations, which include chest skeleton fractures. The JSRT benchmark comprises 247 grayscale X-ray images, each with a resolution of 2048x2048 pixels and a bit depth of 12 bits per pixel. The images are annotated for the presence or absence of lung nodules.

B. Experimental Details

In this study, we trained our model on the NIH ChestX-ray14 dataset, due to memory constraints and computational

requirements, the images were cropped into smaller patches. Specifically, we cropped the dataset into 512x512-pixel fragments that center around the spinal cord region. This allowed us to primarily focus on the spinal cord and a small part of the lungs. However, small details and structures in the lungs, such as capillaries, lesions, and bronchioles, might not be accurately captured by the network when using cropped images.

To evaluate our results, we further cropped the data into 260x512 px fragments to isolate the spinal region from the noise of lung areas. We trained the model on 10,000 randomly selected images and tested it on 1000 randomly sampled images. The experiments were carried out using the PyTorch framework and executed on an NVIDIA Tesla T4 GPU with a batch size of 8. The Adam optimizer was employed with a learning rate of 0.001, $\beta_1 = 0.9$, and $\beta_2 = 0.99$. The model was run for 400 epochs.

To account for the higher magnitude of the gradient correlation loss (Eq. 11) over the feature enhancement loss (Eq. 8), we scaled the contributions of both losses using hyper-parameters $\lambda_2 = 0.001$ and $\lambda_1 = 1$. The experimental results presented in Figure 9 demonstrate that despite the low value of λ , the gradient correlation loss significantly influenced the overall loss.

C. Model evaluation

In this study, we utilized the Blind/Referenceless Image Spatial Quality Evaluator (BRISQUE)[27] and Local Phase Coherence (LPC-SI)[28] metrics to assess the perceptual image quality and image sharpness.

The BRISQUE metric is commonly utilized to assess an image's perceived quality. Its underlying methodology involves comparing an image's pixel statistics to those of a collection of natural images, thereby measuring the degree to which an image deviates from naturalness. To facilitate this comparison, the image is preprocessed by computing MSCN (Mean-Subtracted Contrast-Normalized) coefficients via a non-linear operation detailed in Eq. 13. This procedure enables the statistical properties of the image, including its local contrasts, to be captured.

$$I_{i,j} = \frac{I_{i,j} - \mu_{i,j}}{\sigma_{i,j} + C} \quad (13)$$

where $I_{i,j}$ image pixel, $\mu_{i,j}$ local mean, $\sigma_{i,j}$ local variance, and $C = 1$ is a constant that prevents division by zero.

$$\mu(i,j) = \sum_{k=-K}^K \sum_{l=-L}^L w_{k,l} I(i+k, j+l) \quad (14)$$

$$\sigma(i,j) = \sqrt{\sum_{k=-K}^K \sum_{l=-L}^L w_{k,l} (I(i+k, j+l) - \mu(i,j))^2} \quad (15)$$

where $w = \{w_{k,l} | k = -K \dots K, l = -L \dots L\}$ denotes a 2D circularly-symmetric Gaussian weighting filter. In the implementation, the values of K and L are set to 3. To model the statistical distribution of the MSCN, using a function based on the generalized Gaussian distribution (GGD):

$$f(x; \gamma, \sigma^2) = \frac{\gamma}{2\phi\Gamma(1/\gamma)} \exp\left(-\left(\frac{|x|}{\phi}\right)^\gamma\right) \quad (16)$$

$$\phi = \frac{\sigma}{\Sigma\left(\frac{1}{\gamma}\right) / \Sigma\left(\frac{3}{\gamma}\right)} \quad (17)$$

where $\Gamma(\cdot)$ is the gamma function, γ is the shape parameter that controls the Gaussian shape of the MSCN distribution, and the σ^2 parameter controls the variance. The parameters of $GGD(\gamma, \sigma^2)$ are determined according to a statistical moment matching based approach.

In order to map the statistical characteristics of image content to a quality score, a regression model such as support vector regression (SVR) is employed. The resulting BRISQUE score ranges from 0 to 100, with lower scores indicating higher image quality.

To evaluate the sharpness of an image, we used the LPC-SI algorithm as a no-reference sharpness evaluation technique. This algorithm assesses the coherence among local phase values in the image at different spatial locations to determine its sharpness. The LPC-SI algorithm involves passing the image through a series of N' -scale M' -orientation log-Gabor filters, which are designed to detect features and edges oriented in different directions. The LPC strength at the k -th spatial location and the j -th orientation, and is then computed as:

$$S_{LPS}^k = \frac{\sum_{j=1}^{M'} |c_{1,j,k}| S_{LPC}^{j,k}}{\sum_{j=1}^{M'} |c_{1,j,k}| + C} \quad (18)$$

where M' is the number of the orientations, $|c_{1,j,k}|$ is the first (finest) scale coefficient at j -th orientation and k -the spatial location. The C is a small constant for the numerical stability. The overall LPC-SI is calculated using a weighted averaging method based on the ranked LPC values as:

$$LPC - SI = \frac{\sum_{k=1}^K \eta_k S_{LPC}^k}{\sum_{k=1}^K \eta_k} \quad (19)$$

where S_{LPC}^k is the k -th LPC strength values, and η_k is the weight assigned to the S_{LPC}^k value.

The LPC-SI metric utilizes a weight that is assigned to each LPC strength value based on its rank. This weighting scheme is designed to modify the degree of influence that each individual LPC strength value effect on the overall LPC-SI measure.

$$\eta_k = \exp\left[-(1 - \frac{k}{K})/\rho_k\right] \quad (20)$$

where K is a number of spatial locations, and the parameter ρ is controlling the speed of decaying of the weight. All parameters are set empirically.

A high value of LPC-SI indicates a high sharpness.

D. Experimental Results

Our model's performance was assessed both visually and quantitatively, and we compared it against two other methods: Madmad [15], which is a learning-based technique for enhancing X-ray image details, and Fattal [14], which is a conventional method based on the Weighted Least Squares (WLS) algorithm.

Quantitative Comparison: Table II displays the quantitative evaluation of our method in comparison to other techniques on three datasets, namely NIH ChestX-ray14, CheXpert, and JSRT. The results reveal that BRISQUE yield the most promising outcomes on three of datasets and in terms of LPC-SI, they are comparable to Fattal's method on the NIH ChestX-ray14 dataset.

Qualitative Comparison: In this study, we compared the proposed method with existing techniques for enhancing image details. We present the comparison results in Figure 8 on tested datasets, namely NIH ChestX-ray14, JSRT, and CheXpert. The first two rows of images from NIH ChestX-ray14 and the third row from JSRT datasets show enhancement of the hardly visible details of the spinal regions. The fourth and fifth rows represent the frontal and lateral views of the same image from the CheXpert dataset. To emphasize the clinical significance of our research, we selected images from this dataset annotated with fractures. Specifically, we chose images with fractures in the spinal region where also the radiologist's report indicated a reduction in vertebral height. This comparison demonstrates our method's ability to learn more latent features and emphasize geometric structures, resulting

from the integration of all model components.

E. Expert Assessment Results

To evaluate the effectiveness of our proposed model from a professional standpoint, we sought the opinion of two expert radiologists. The assessment was performed on four sets of 71 randomly selected X-ray images from three different datasets, with each set containing our enhanced results, Fattal's results, Madmad's results, and an audit set with original images. The radiologists were blinded to which images were processed by our model and were asked to rank each image in the sets on a scale of 1 to 3, with 1 indicating the highest-quality image and 3 indicating the lowest-quality image. The ranked scores were summarized in Table I, which reveals that our method received the highest grade from both radiologists.

Table I: Radiologist's assessment cumulative rating scale

Scores	Radiologist 1			Radiologist 2		
	Fattal	Madmad	Ours	Fattal	Madmad	Ours
1	8.7 %	34.8%	56.5%	32.4%	43.7%	53.5%
2	17.4%	56.5%	26.1%	35.2%	42.3%	21.1%
3	73.9%	8.7%	17.4%	32.4%	14.1%	25.4%

F. Ablation Analysis

In the following experiments, we conducted an ablation analysis to assess the influence of various components of the proposed methodology.

Effect of the Guidance Layer: In order to examine the efficacy of the guidance layer, we performed a comparative analysis of the model's output with and without the guidance layer, as presented in Figure 5. The model was trained only once to eliminate the influence of multiple iterative steps or optimized losses. The difference between the network output image and the original image was evaluated using the ℓ_2 loss, enabling us to assess the impact of the guidance layer without the effect of the optimized loss.

The results in Figure 5 reveal that the guidance layer supplies supplementary information to low-level features, thus enhancing detail visualization. Furthermore, we investigated the effect of training the network solely with a detail layer as the guidance layer. However, this approach did not yield significant improvements and produced similar results to training without the guidance layer.

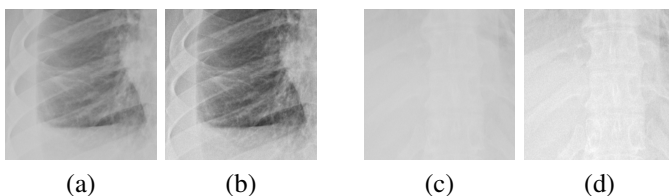


Figure 5: Comparison of the different fragments of the same image with and without guidance layer, where (a) and (c) are fragments of the original image to corresponding fragments of the recovered image (b) and (d).

Optimized Loss: To evaluate the individual contributions of the details enhancement loss (DEL) and gradient correlation loss (GCL), the model was trained using different configurations. The results of the quantitative analysis are presented in Table II. First, we examined the effect of DEL. We replaced the DEL with an ℓ_2 loss which receives the processed and original images as inputs. Thus, we didn't get featured images but rather original ones. Similarly, to evaluate the impact of GCL on the object's contours, an ℓ_2 loss was used instead of GCL, which receives the processed image and details layer. The results of this experiment are shown in Table II and Figure 6, where comparable BRISQUE scores were observed between the models trained using a combined GCL and DEL losses and those trained using a combination of GCL and ℓ_2 loss.

Table II: Comparison of model with different loss settings (MEAN \pm STD)

Methods	BRISQUE	LPC-SI
ℓ_2 +DEL	21.634 \pm 8.619	0.871 \pm 0.056
GCL+ ℓ_2	21.201 \pm 8.176	0.883 \pm 0.051
GCL+DEL	21.173 \pm 10.169	0.889 \pm 0.048

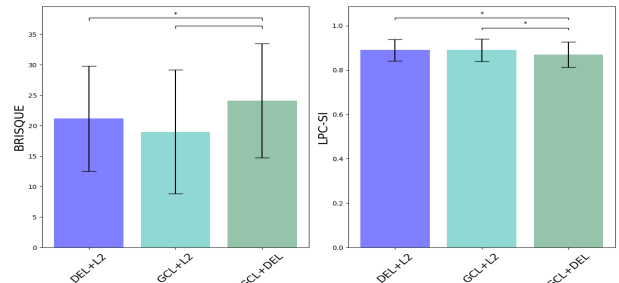


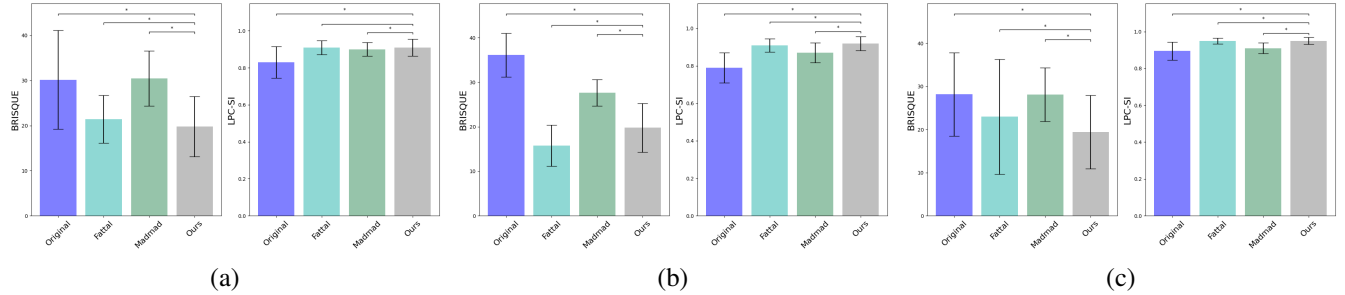
Figure 6: A bar and whisker plot show results of the BRISQUE and LPC-SI metrics for different loss settings. The Wilcoxon signed-rank test was used to examine the difference between loss settings. * - Statistical significance at $p < 0.05$

Effect of iterative training: To examine effect of the iterative training we repeated the training process three times. Nevertheless, after two training sessions, we observed that the model generated over-enhanced outputs, including various artifacts that affected image quality and feature consistency. This finding was supported by the clinicians' visual examination and by the quantitative metrics. Table IV and Figure 10 present the quantitative outcomes comparing the first and second training sessions. The results demonstrate an enhancement in all metric scores, implying a more precise representation of the perceptual connections between structures in the image.

¹Implementation of methods that have been compared:
Fattal: <https://www.cs.huji.ac.il/~danix/epd/>
Madmad:<https://github.com/tahanimadmad/CNN-Based-X-ray-\Morphological-Decomposition->

Table III: Comparison between traditional and learning-based methods by image quality assessments (MEAN \pm STD)

Datasets	NIH Chest X-rays		JSRT		CheXpert	
Methods	BRISQUE	LPC-SI	BRISQUE	LPC-SI	BRISQUE	LPC-SI
Original	29.076 \pm 10.959	0.820 \pm 0.084	35.626 \pm 4.941	0.813 \pm 0.081	28.310 \pm 9.635	0.887 \pm 0.049
Fattal	24.089 \pm 4.611	0.910 \pm 0.037	24.263 \pm 4.901	0.914 \pm 0.036	26.748 \pm 13.348	0.945 \pm 0.016
Madmad	28.930 \pm 6.065	0.893 \pm 0.037	28.556 \pm 4.451	0.885 \pm 0.053	28.148 \pm 6.215	0.907 \pm 0.028
Ours	19.881 \pm 6.675	0.910 \pm 0.044	19.545 \pm 5.487	0.922 \pm 0.037	21.195 \pm 8.507	0.950 \pm 0.030

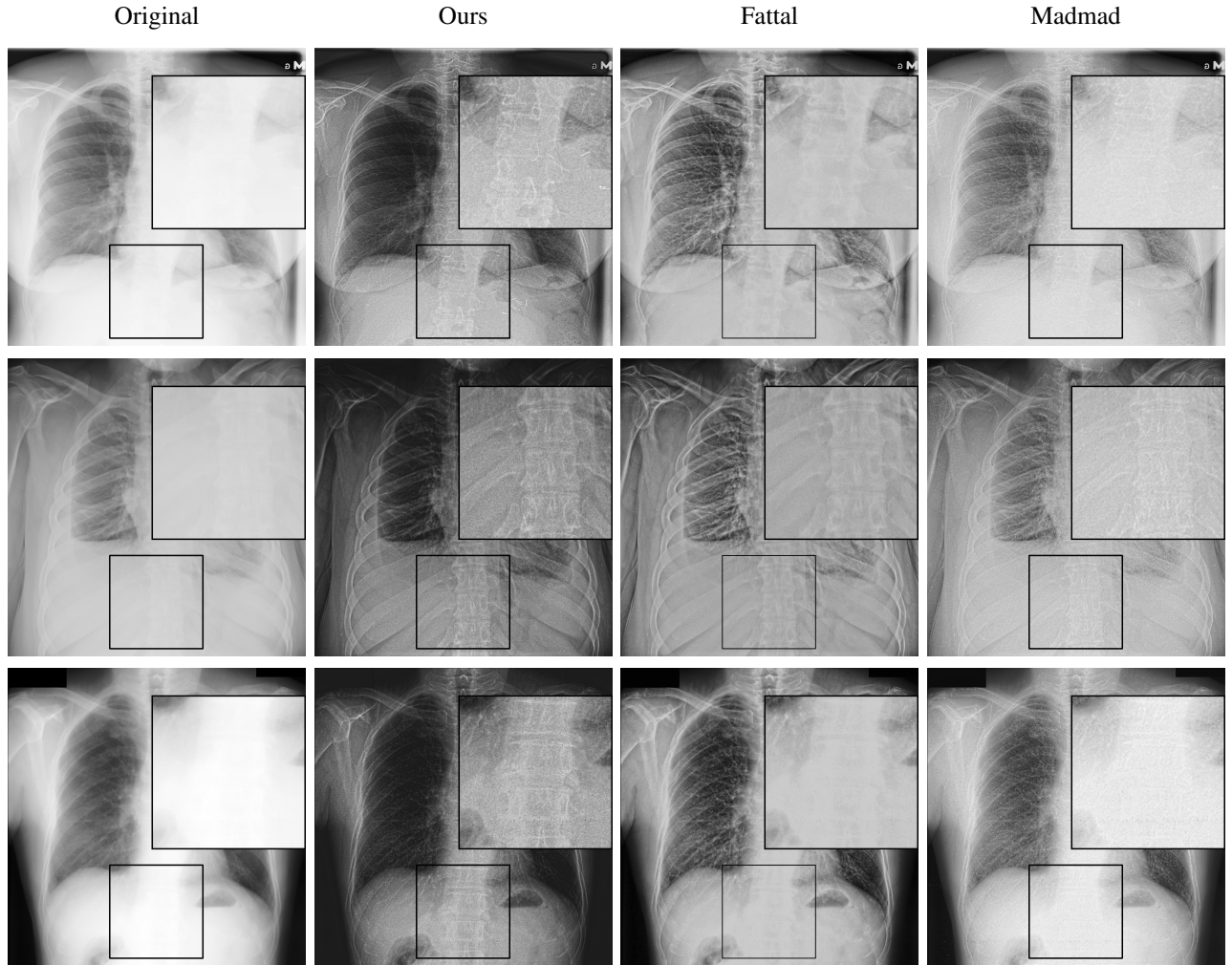


(a)

(b)

(c)

Figure 7: A bar and whisker plot show the results of the BRISQUE and LPC-SI metrics across different methods evaluated on three datasets: (a) the NIH Chest X-rays dataset (b) the JSRT dataset (c) and the results of the CheXpert dataset. The Wilcoxon signed-rank test was used to compare the differences between the compared method's assessment scores and the proposed method. * - Statistical significance at $p < 0.05$.



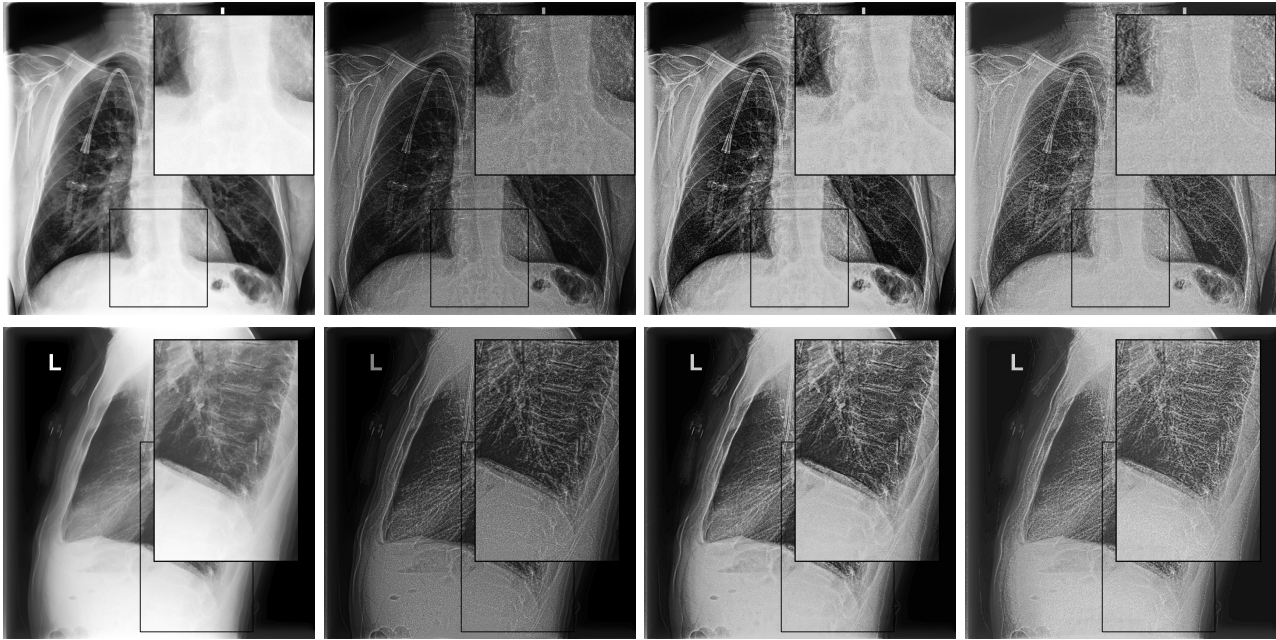


Figure 8: Qualitative comparison of image enhancement methods on three datasets: NIH Chest X-ray, JSRT, and CheXpert. The first two rows show results from the NIH Chest X-ray dataset, the third row shows data from the JSRT dataset, and the last two rows show data from the CheXpert dataset.

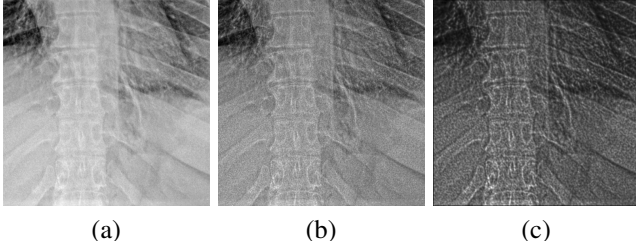


Figure 9: A comparison of the outputs after three training steps: (a) First step (b) Second step (c) Third step

Table IV: Comparison between one and two iterations of learning (MEAN \pm STD)

Methods	BRISQUE	LPC-SI
First step	20.680 ± 7.886	0.891 ± 0.055
Second step	19.881 ± 6.675	0.910 ± 0.044

Effect of preprocessing method: To assess the impact of the preprocessing method on the final results, we conducted two training sessions: one without preprocessing and another with preprocessing. The quantitative and qualitative results presented in Table V and Figure 11 respectively, demonstrate that data preprocessing significantly contributes to identifying and learning implicit features.

V. CONCLUSIONS

In this study, we introduced a robust approach to significantly enhance the thoracic spine in chest X-ray images.

We rigorously evaluated the robustness and efficacy of our method through comprehensive quantitative and qualitative

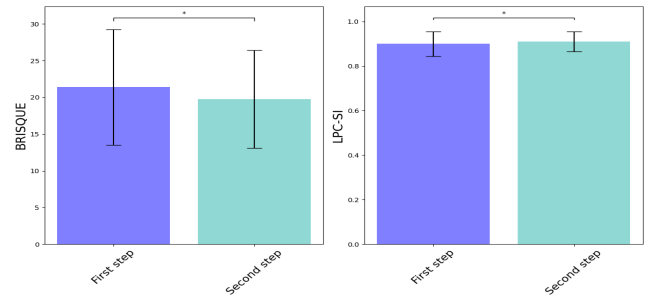


Figure 10: A box and whisker plot was used to display assessment scores for the results after the first and second learning steps. The Wilcoxon rank test examines the significance of the results after each step.* - Statistical significance at $p < 0.05$.

Table V: Statistical results of data with and without preprocessing technique (MEAN \pm STD)

Methods	BRISQUE	LPC-SI
Original	29.076 ± 10.959	0.820 ± 0.084
Preprocessed	26.394 ± 11.275	0.833 ± 0.084
Learning-based	24.517 ± 5.462	0.875 ± 0.058
Prep.+Learning	19.881 ± 6.674	0.910 ± 0.044

assessments, surpassing two other existing techniques, namely Fattal and Madmad, for X-ray image enhancement. Our method demonstrated exceptional performance across various quantitative metrics, including detail appearance, perceived quality, and sharpness, when evaluated on the NIH Chest X-rays, JSRT and CheXpert datasets. Furthermore, our

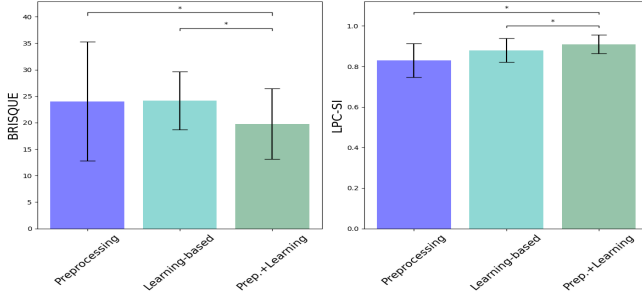


Figure 11: The plotted assessment metric scores using a bar and whisker plot for different model components: preprocessing, learning-based method, and their combination. The effect of each component on the data was examined using the Wilcoxon rank test. * - Statistical significance at $p < 0.05$.

method exhibited better performance in terms of perceived quality and sharpness on the JSRT and CheXpert datasets and was comparable in terms of LPC-SI on the NIH Chest X-rays dataset. Finally, our model demonstrated clinical significance on the CheXpert dataset by identifying poor visibility of spinal lesions.

Acknowledgements: We would like to thank Dr. Mohammad Badarne, a radiologist from Wolfson Medical Center, and Dr. Hila Rozen from Hadassah Medical Center for providing clinical advice, guidance, and assessing the technique’s performance in improving the X-ray images.

REFERENCES

- J. He, M. Chen, Z. Li , “Edge-aware Local Laplacian Filters for Medical X-Ray Image Enhancement,” in *International Conference on Health Information Science*, pp. 102–108, 2016.
- I. Ikhсан, A. Hussain, M. Zulkifley, N. Tahir, A. Mustapha, “An analysis of x-ray image enhancement methods for vertebral bone segmentation,” in *IEEE 10th International Colloquium on Signal Processing and its Applications 2014*, pp. 208–211, 2014.
- S. M. Pizer, R. E. Johnston, J. P. Ericksen, B. C. Yankaskas, and K. E. Muller, “Contrast-limited adaptive histogram equalization: speed and effectiveness,” in *Proceedings of Conference on Visualization in Biomedical Computing*, pp. 337–345, 1990.
- M. Sundaram, K. Ramar, N. Arumugam, and G. Prabin, “Histogram modified local contrast enhancement for mammogram images,” in *Applied Soft Computing*, vol. 11, no. 8, pp. 5809–5816, 2011.
- Q. Lyu, H. Shan, C. Steber, C. Helis, C. T. Whitlow, M. Chan, and G. Wang, “Multi-Contrast Super-Resolution MRI Through a Progressive Network,” in *IEEE Transactions on Medical Imaging*, pp. 2738–2749, 2020.
- C. Dong, C. C. Loy, K. He, X. Tang, “Image super-resolution using deep convolutional networks,” in *IEEE Transactions on Pattern Analysis and Machine Intelligence (PAMI) 38*, vol. 11, no. 8, pp. 5809–5816, 2016.
- B. Lim, S. Son, H. Kim, S. Nah, and K. Mu Lee, “Enhanced Deep Residual Networks for Single Image Super-Resolution,” in *IEEE Conference on Computer Vision and Pattern Recognition Workshops*, pp. 136–144, 2017.
- W.-S. Lai, J.-B. Huang, N. Ahuja, and M.-H. Yang, “Deep Laplacian Pyramid Networks for Fast and Accurate Super-Resolution,” in *IEEE International Conference on Computer Vision*, pp. 5835–5843, 2017.
- A. Shocher, N. Cohen, M. Irani, “Zero-Shot” Super-Resolution using Deep Internal Learning,” in *IEEE Conference on Computer Vision and Pattern Recognition*, pp. 3118–3126, 2018.
- Y. Yuan, S. Liu, J. Zhang, Y. Zhang, C. Dong, and L. Lin, “Unsupervised image super-resolution using cycle-in-cycle generative adversarial networks,” in *IEEE Conference on Computer Vision and Pattern Recognition Workshops*, pp. 814–823, 2018.
- Z.-S. Liu, W.-C. Siu, L.-W. Wang, C.-T. Li, and M.-P. Cani, “Unsupervised Real Image Super-Resolution via Generative Variational AutoEncoder,” in *IEEE Conference on Computer Vision and Pattern Recognition Workshops*, pp. 442–443, 2020.
- O. Gozes, H. Greenspan, “Bone structures extraction and enhancement in chest radiographs via CNN trained on synthetic data,” in *IEEE 17th International Symposium on Biomedical Imaging (ISBI)*, pp. 858–861, 2020.
- Q. M. Ali, Z. Yan, H. Li, “Iterative Thresholded Bi-Histogram Equalization for Medical Image Enhancement,” in *International Journal of Computer Applications*, 2015.
- Z. Farbman, R. Fattal, D. Lischinski, R. Szeliski, “Edge-preserving decompositions for multi-scale tone and detail manipulation,” in *ACM Trans. Graph.*, vol. 27, no. 3, pp. 249–256, 2008.
- T. Madmad, N. Delinte, C. De Vleeschouwer, “CNN-based morphological decomposition of X-ray images for details and defects contrast enhancement,” in *IEEE/CVF Conference on Computer Vision and Pattern Recognition*, pp. 2170–2180, 2021.
- I. I. J. Sander, B. D. de Vos, “Unsupervised Super-Resolution: Creating High-Resolution Medical Images from Low-Resolution Anisotropic Examples,” in *Medical Imaging*, vol. 11596, p. 115960E, 2021.
- C. Ma, Y. Rao, Y. Cheng, C. Chen, J. Lu, and J. Zhou, “Structure-Preserving Super Resolution with Gradient Guidance,” in *IEEE Conference on Computer Vision and Pattern Recognition*, pp. 7766–7775, 2020.
- D. Lischinski, Z. Farbman, M. Uyttendaele, R. Szeliski, “Interactive local adjustment of tonal values,” in *ACM Transactions on Graphics (TOG)*, vol. 25, pp. 646–653, 2006.
- O. Ronneberger, P. Fischer, and T. Brox, “U-net: Convolutional networks for biomedical image segmentation,” in *MICCAI*, pp. 234–241, 2015.
- P. L. K. Ding, Z. Li, Y. Zhou, and B. Li, “Deep Residual Dense U-Net for Resolution Enhancement in Accelerated MRI Acquisition,” *Medical Imaging 2019: Image Processing*, vol. 10949, pp. 110–117, 2019.
- S. Ai and J. Kwon, “Extreme Low-Light Image Enhancement for Surveillance Cameras Using Attention U-Net,” in *Sensors*, vol. 20, no. 2, p. 495, 2019.
- G. P. Penney, J. Weese, J. A. Little, P. Desmedt, D. L. G. Hill, and D. J. Hawkes, “A comparison of similarity measures for use in 2-D-3-D medical image registration,” in *IEEE transactions on medical imaging*, pp. 586–595, 1998.
- Y. Hiasa, Y. Otake, M. Takao, T. Matsuoka, K. Takashima, A. Carass, J. Prince, N. Sugano, and Y. Sato, “Cross-modality image synthesis from unpaired data using CycleGAN,” in *International Workshop on Simulation and Synthesis in Medical Imaging*, pp. 31–41, 2018.
- X. Wang, Y. Peng, L. Lu, and R. Summers, “Chestx-ray8: Hospital-scale chest x-ray database and benchmarks on weakly-supervised classification and localization of common thorax diseases,” in *IEEE Conference on Computer Vision and Pattern Recognition*, pp. 2097–2106, 2017.
- J. Irvin, P. Rajpurkar, M. Ko, Y. Yu, S. Ciurea-Ilcus et al., “CheXpert: A Large Chest Radiograph Dataset with Uncertainty Labels and Expert Comparison,” in *In AAAI Conference on Artificial Intelligence*.
- J. Shiraishi, S. Katsuragawa, J. Ikezoe, T. Matsumoto, T. Kobayashi, K.-i. Komatsu, M. Matsui, H. Fujita, Y. Kodera, and K. Doi, “Development of a digital image database for chest radiographs with and without a lung nodule,” in *American Journal of Roentgenology*, vol. 174, no. 1, pp. 71–74, 2000.
- A. Mittal, R. Soundararajan, and A. C. Bovik, “No-Reference Image Quality Assessment in the Spatial Domain,” in *IEEE Transactions on Image Processing*, no. 12, pp. 4695–4708, 2012.
- R. Hassen, Z. Wang, and M. M. Salama, “Image sharpness assessment based on local phase coherence,” in *IEEE Transactions Image Processing*, vol. 22, no. 7, pp. 2798–2810, 2013.